A 3D-model inversion of methyl chloroform to constrain the atmospheric oxidative capacity

Stijn Naus[1], Stephen A. Montzka[2], Prabir K. Patra[3,4], and Maarten C. Krol[1,5]

[1]Meteorology and Air Quality, Wageningen University and Research, the Netherlands
[2]NOAA Global Monitoring Laboratory, Boulder, CO, USA
[3]Research Institute for Global Change, JAMSTEC, Yokohama, Japan
[4]Center for Environmental Remote Sensing, Chiba University, Chiba, Japan
[5]Institute for Marine and Atmospheric Research, Utrecht University, the Netherlands

Correspondence: Stijn Naus (stijn.naus@wur.nl)

Abstract. Variations in the atmospheric oxidative capacity, largely determined by variations in the hydroxyl radical (OH), form a key uncertainty in many greenhouse and other pollutant budgets, such as that of methane (CH_4). Methyl chloroform (MCF) is an often-adopted tracer to indirectly put observational constraints on variations in OH. We investigated the budget of MCF in a 4DVAR inversion using the atmospheric transport model TM5, for the period 1998-2018, with the objective to derive

5   information on interannual variations in OH and in its spatial distribution.

We derived interannual variations in the global oxidation of MCF that bring simulated mole fractions of MCF within 1-2% of the assimilated observations from the NOAA-GMD surface network at most sites. Additionally, the posterior simulations better reproduce aircraft observations used for independent validation. The derived OH variations showed robustness with respect to the prior MCF emissions and the prior OH distribution. The interannual variations were typically small (<3%/year), with no

10   significant longterm trend in OH.

The inverse system found strong adjustments of the latitudinal distribution of OH, with systematic increases in tropical OH and decreases in extra-tropical OH (both up to 30%). These spatial adjustments were driven by intrahemispheric biases in simulated MCF mole fractions, which have not been identified in previous studies. Given the unexpectedly large amplitude of these adjustments and a residual bias in intrahemispheric gradients, we suggest a reversal in the extratropical ocean sink of

15   MCF in response to declining atmospheric MCF abundance (as hypothesized in Wennberg et al. (2004)). This reversal provides a more realistic explanation for the biases, possibly complimentary to adjustments in the OH distribution.

While we identified significant added value in the use of a 3D transport model over simpler box models, we also found a trade-off in computational expense and convergence problems. However, although the signals are small compared to assuming interannually repeating OH, the derived variations better match the global MCF observations and are relevant for studying the

20   budget of e.g. CH_4.

1 Introduction

The hydroxyl radical (OH) is the main atmospheric oxidant and plays an integral role in atmospheric chemistry. OH is involved in the removal of a wide variety of toxic pollutants (carbon monoxide, nitrogen oxides), greenhouse gases (e.g. methane (CH_4) and HFC's) and gases that contribute to stratospheric ozone depletion (various HCFC's). Therefore, in order to better

25 understand and constrain these different pollutant budgets, robust constraints on OH are required.

Due to its high reactivity, OH has a short atmospheric lifetime of seconds and is present at low abundances in the atmosphere. This makes direct measurements of OH difficult, and extrapolation of these measurements to global scales near impossible. Bottom-up modeling of OH in full-chemistry models is a useful tool to better understand the OH budget. However, this modeling relies on accurate understanding of the complex chemistry involved and of the emissions of many species, and it lacks

30 observational constraints. A third approach to constrain OH is to indirectly estimate atmospheric oxidation from observed variations in the growth rate of a tracer removed by OH. This "proxy"-method can provide independent observational constraints on OH on large spatio-temporal scales, against which the understanding implemented in full-chemistry models can be tested.

Different species have been proposed and used to constrain OH. The most widely adopted of these is methyl chloroform (MCF). MCF was used as a solvent up to the early 1990s, after which its production was phased out in the Montreal Protocol and

35 its subsequent amendments. MCF is predominantly removed through oxidation by OH, with secondary sinks by stratospheric photolysis and oceanic hydrolysis, resulting in an atmospheric lifetime of 5-6 years (Chipperfield and Liang, 2013). As MCF is emitted purely anthropogenically and its production is thought to be well-constrained, MCF was identified early on as a potential tracer for OH (Lovelock, 1977; Prinn et al., 1987). This potential improved after the production phase-out and the rapid emission decline, as the MCF budget became dominated by its OH sink. The combination of a period with well-

40 constrained production, followed by a period with a small role of its emissions, makes MCF a good tracer for OH.

Study of the MCF budget has provided important insights into the atmospheric distribution of OH and temporal variations therein. For example, observations of MCF were used to quantify a likely upper limit to interannual variations in global mean OH of 2-3% (Montzka et al., 2011), which is in line with full-chemistry models. On the other hand, whereas chemistry models typically find higher OH concentrations in the Northern than in the Southern Hemisphere, a modeling study found MCF

45 observations to be most consistent with interhemispheric parity (Patra et al., 2014).

Use of MCF to constrain OH is not without challenges, however. Through improvements in measurement techniques, measurement quality has mostly kept pace with the atmospheric decline of MCF, but artifact-free sampling has become more difficult. Additionally, a decline of the atmospheric burden implies an increasingly important role of any small, persistent emissions in the MCF budget. As a further complication, atmospheric decline of MCF has been suggested to result in a reversal

50 of the small but significant ocean sink of MCF at high latitudes (Wennberg et al., 2004). Finally, the surface measurement networks that monitor MCF are relatively sparse and thus they provide limited capacity to distinguish one budget term from another.

These limitations were emphasized in two recent studies that constrained interannual variations of OH in a two-/three-box model of MCF and CH_4 (Turner et al., 2017; Rigby et al., 2017). In their most likely solution, both studies suggested the

55 possibility for an important contribution from OH to CH$_4$ growth rate variations. However, the looseness of derived constraints on OH variations also allowed for a solution with no variations in OH. In an extension of these studies, we investigated in previous work how the use of a relatively simple box model, rather than a more sophisticated 3D transport model, could have affected these conclusions (Naus et al., 2019). We found that large changes in the MCF budget over time (i.e. the sudden drop in its emissions) resulted in significant changes in, for example, interhemispheric transport of MCF and the stratospheric MCF

60 sink. However, accounting for these changes in our two-box model did not alter the conclusion that MCF-derived constraints on multi-annual variations of OH are too uncertain to determine the exact contribution of OH to the relatively small but important CH$_4$ growth rate variations.

In this study, we present an inversion of MCF in the 3D chemistry-transport model TM5 aimed at constraining OH. The advantage of approaching the problem in a 3D transport model, instead of in a box model, is two-fold. Firstly, by explicitly

65 resolving transport, we avoid the transport biases that hamper simple box models. Secondly, we can fully exploit the available observations and the gradients between surface sites. For example, since MCF is predominantly removed in the tropics, the latitudinal distribution of MCF has had a tropical minimum since 1998 (Spivakovsky et al., 2000; Montzka et al., 2000). There is potential for this type of information to provide constraints on OH that has not been exploited by box-model approaches.

The last comprehensive 3D model OH-inversion of MCF investigated the 1980-2000 period (Bousquet et al., 2005). Here,

70 we instead cover the 1998-2018 period. An important difference between these two periods concerns the role of emissions. The 1980-2000 period includes a period with high MCF emissions, as well as the subsequent strong decrease in emissions from 1990 onward, which complicated the interpretation of MCF observations. Contrastingly, the situation over 1998-2018 was simpler, with a near-constant exponential decline of atmospheric MCF and a small role for its emissions.

The objective of this study is to investigate information on large-scale OH variations contained in measurements of the most

75 promising tracer identified to date, MCF, in the most promising period in its measured history, the period after its drop in emissions, using the most comprehensive tools available to us, in the form of a state-of-the-art inverse system built around a 3D transport model.

2 Methods

2.1 Inverse method

80 #### 2.1.1 TM5-4DVAR

To simulate atmospheric transport, we used the transport model TM5 (Krol et al., 2005). We operated TM5 on a 6° by 4° horizontal resolution, with 25 vertical layers. Transport in TM5 was driven by offline meteorological fields from the ERA-Interim reanalysis from the European Centre for Medium Range Weather Forecasts (ECMWF) (Dee et al., 2011).

For optimization of OH and other parameters, we used the inversion framework TM5-4DVAR (Meirink et al., 2008). TM5-

85 4DVAR is an inverse system based on the variational optimization technique 4DVAR. TM5-4DVAR has been applied successfully in previous studies to a variety of problems, such as to constrain the global CH$_4$ budget (Bergamaschi et al., 2009) and

to investigate the Indonesian wildfires (Nechita-Banda et al., 2018). The objective of our set-up of the TM5-4DVAR inverse system is to find the optimal configuration of MCF emissions and OH variations that best reproduce atmospheric observations of MCF. Formally, this objective is quantified as minimization of the cost function J (Equation 1).

90

$$J(\boldsymbol{x}) = \frac{1}{2}(\boldsymbol{x} - \boldsymbol{x}_{prior})^T \mathbf{B}^{-1}(\boldsymbol{x} - \boldsymbol{x}_{prior}) + \frac{1}{2}(\mathbf{H}\boldsymbol{x} - \boldsymbol{y})^T \mathbf{R}^{-1}(\mathbf{H}\boldsymbol{x} - \boldsymbol{y}). \qquad (1)$$

J is a function of the state $\boldsymbol{x}$, which contains all the parameters to be optimized, such as OH. The cost consists of two terms. First is the deviation from the first guess x_{prior}, weighted by the prior error covariance matrix $\mathbf{B}$. Second is the difference between simulated MCF mole fractions, calculated in the forward version of TM5 (denoted as $\mathbf{H}$), and the real-world observations $\boldsymbol{y}$, weighted by the observational covariance matrix $\mathbf{R}$. Additionally, in the 4DVAR optimization, the gradient of the cost

95   function ∇J is calculated and used (Equation 2).

$$\nabla J(\boldsymbol{x}) = \mathbf{B}^{-1}(\boldsymbol{x} - \boldsymbol{x}_{pri}) + \mathbf{H}^\mathbf{T}\mathbf{R}^{-1}(\mathbf{H}\boldsymbol{x} - \boldsymbol{y}), \qquad (2)$$

with $\mathbf{H}^\mathbf{T}$ the adjoint of the forward model $\mathbf{H}$. The adjoint of TM5 is extensively described in Meirink et al. (2008) and Krol et al. (2008). Since OH chemistry is non-linear and since we optimized emissions non-linearly (see Section 2.1.2), $\mathbf{H}^\mathbf{T}$ is actually the adjoint of the forward tangent linear model. The derivation of the adjoint OH chemistry is described in Supplement

100   S5.

2.1.2 Inversion set-up

In this section we discuss the set-up of the three inversions we performed. First we describe the set-up of the standard inversion (hereafter referred to as REF); next we describe the corresponding $\mathbf{B}$ matrix; finally we describe the two variations of the standard inversion which we performed. Note that the $\mathbf{R}$ matrix is discussed in Section 2.2.

105   In the standard inversion, we used the MCF source and sink fields from the TransCom-CH4 project (Patra et al., 2011). Loss fields for OH, stratospheric photolysis and ocean uptake are described in the TransCom-CH$_4$ protocol. Briefly, the OH fields are a combination of tropospheric OH fields from Spivakovsky et al. (2000), scaled by a factor 0.92, and stratospheric OH fields derived with the 2D MPIC chemistry model (Brühl and Crutzen, 1993). The ocean flux is a first-order sink proportional to MCF mole fractions in the lowest model layer and a spatially variable uptake rate, which maximizes in the tropics. Stratospheric

110   photolysis fields were generated with simulations of the ACTM model (Patra et al., 2009). TransCom MCF emissions were available only up to 2006. In subsequent years, we repeated the 2006 spatial distribution. We pre-optimized annual total MCF emissions to approximately reproduce global mean MCF mole fractions, as derived from the NOAA surface network, assuming no interannual variations in OH. The procedures to obtain hemispheric and global mean MCF mole fractions from the NOAA surface network are extensively described in Supplement S1 of Naus et al. (2019).

115   We included both OH and MCF emissions in the state vector for optimization. Emissions were optimized monthly in each grid box with an assumed grid-box error of 50%, and with a horizontal correlation length of 500 kilometres and a temporal

correlation of 9.5 months. In the construction of the **B**-matrix, OH fields were optimized monthly, in 45 latitudinal bands (i.e. on our native latitudinal resolution), with an error per band of 10%. We imposed high correlations between the latitudinal bands of 0.8 (corresponding to a correlation length of 1500-2000 km), and a temporal correlation length of 12 months. Since

120 there are fewer state elements for OH than for emissions, we increased the cost of adjusting OH relative to that of adjusting emissions by an additional factor 5, similar to e.g. Maasakkers et al. (2019). This adjustment ensures that the cost of adjusting total emissions or global mean OH by 1σ of the global uncertainty is comparable.

Both OH and emissions were optimized with non-linear scaling factors, which preclude negative emissions and OH concentrations. This method was introduced in Bergamaschi et al. (2009) and we describe it more extensively in Supplement S5. Due

125 to the non-linear nature of this inverse problem, we use the M1QN3 solver (Gilbert and Lemaréchal, 1989). The downside of this choice is that we cannot retrieve the posterior covariance matrix. We instead tested the robustness of derived solutions with respect to the OH and the emission distribution, two very likely sources of uncertainty, in two additional inversions.

In our second inversion, referred to as POP, we redistributed the same annual total MCF emissions as in the REF inversion proportional to population density (as retrieved from CIESIN, Columbia University (2018)). In the third inversion (referred

130 to as TM5OH), we used the same emissions as in the REF inversion, but adopted a tropospheric OH distribution based on a simulation of the year 2006 performed with the full-chemistry version of TM5 (Huijnen et al., 2010), combined with the same stratospheric distribution as in the standard inversion. Differences between the two OH distributions are typically 10-15%, depending on the latitude. The TM5OH distribution has relatively higher OH concentrations in the Northern hemisphere.

On a final note, while we optimized scaling factors for OH per latitudinal band, we prefer to discuss the change in global

135 mean oxidation in further sections, rather than the change in global mean OH. We quantified the change in oxidation as the atmospheric mass-weighted average of $k(T) \cdot$OH, with $k(T)$ the temperature-dependent reaction rate between OH and MCF (Burkholder et al., 2015). This is necessary, because we allowed for adjustments in the latitudinal distribution of OH. Since latitude and temperature are strongly correlated, a latitudinal redistribution of OH that conserves global total oxidation often implies a change in global mean OH. In that case, we consider the conservation of global total oxidation the relevant quantity,

140 rather than a change in global mean OH (similar to the recommendation in Lawrence et al. (2001)). We calculate the variations in oxidation relative to the prior, so that for example interannual variations of temperature will not affect these variations in oxidation, since temperature variations remain the same between prior and posterior simulations. Where relevant, we make note of this distinction. We also present results for the latitudinal adjustments in OH.

2.2 Observations

145 ### 2.2.1 Surface observations

We used MCF observations from the surface network of the National Oceanic and Atmospheric Administration (NOAA) Global Monitoring Laboratory (GML) as the only observational constraints in the inversion. The network consists of a core set of 7 surface sites that have monitored MCF since 1992, and additional sites have been added since: data from a total of 12 sites are available since 1998. The sites we used, including site abbreviations, are described in Table S1. At each site, paired

150   flask samples are collected at weekly to monthly frequency, following a sampling protocol that typically favors sampling under meteorological conditions that correspond to clean background air. Flask samples are then collected and measured on one central measurement system against the NOAA calibration scale for MCF. The measurement uncertainties we used are those reported by NOAA, which are based on the difference between the mole fractions measured for each flask in a flask pair. Up to 2018, short-term measurement repeatability remained consistently around 0.5% of the measured mole fraction. On top

155   of the measurement error, we also included a model error that was proportional to the 3D spatial gradients simulated in the atmosphere around the surface sites. Typically, the model error was up to 1% at Northern midlatitude sites (e.g. LEF), and as low as 0.1% at e.g. SPO or ALT. The addition of these two error sources, with no correlations in between, constitute the **R** matrix (see Section 2.1).

2.2.2   Aircraft campaigns

160   For validation of the inversion results, we used two sets of aircraft campaigns: the HIAPER Pole-to-Pole Observations (HIPPO, 2009-2012, Wofsy et al. (2011)) and the Atmospheric Tomography Missions (ATom, 2016-2018, Wofsy et al. (2018)). The five HIPPO campaigns were flown from $85°$N to $67°$S over the Pacific, with vertical profiles being sampled up to 8500 meters at approximately $2.2°$ intervals. The horizontal extent of the ATom campaigns was wider, with global coverage over the Pacific, the Atlantic and the Arctic oceans.

165   While a number of different measurement systems provided measurements of MCF during HIPPO, only results from the NOAA Whole Air Sampler during H-1, -3, -4, and -5 were included in this analysis because they are most closely tied to NOAA's surface network results (i.e., in methodology, precision, and calibration consistency). ATom results from deployments A-2 and A-3 were also included in this work, as those flask samples were analyzed on the same NOAA instrument as the surface network flasks. We exclude from our analysis a subset of results from HIPPO-1, as well as all of HIPPO-2 and the

170   ATom-1 missions, since samples from these deployments suffered from a deployment-specific measurement interference (a portion of H-1 and all of H-2) or were analyzed on a different instrument in NOAA that exhibited poorer precision (A-1).

3   Results

3.1   Variations in the atmospheric oxidative capacity and in MCF emissions

In Figure 1, we show the monthly anomalies in global oxidation (different from global mean OH: see Section 2.1.2), as derived

175   in the three inversion set-ups. We have shown the entire twenty-year inversion period, which will include a spin-up and spin-down period of 1-2 years. For example, even though our initial MCF mole fraction fields are realistic, the strong positive oxidation anomaly in 1998 might be linked to errors in the initial field.

Interannual variations in global oxidation are typically small ($\sim 2\%$). In this, there is consistency between the different inversion set-ups. Variability in the POP and the TM5OH inversions are strongly positively correlated ($R^2 = 0.92$), while the

180   correlation with the REF inversion is weaker ($R^2 = 0.51$). It is counter intuitive that the REF inversion deviates from the other
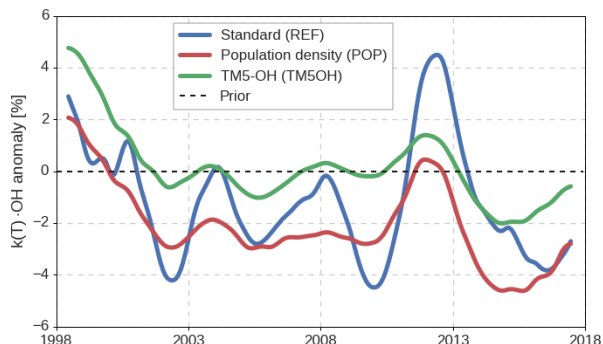
Figure 1. Monthly variations in global mean $k(T) \cdot OH$, derived in the three different inversion set-ups. Variations in $k(T) \cdot OH$ are calculated relative to the prior simulation, thus removing the influence of interannual variations in temperature.
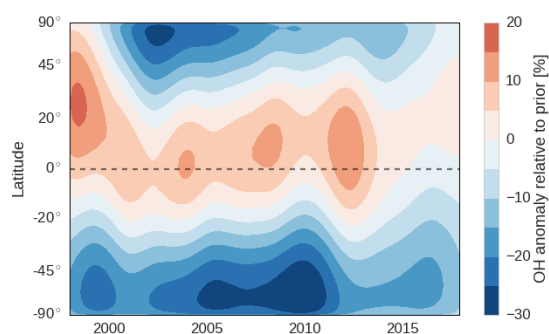
Figure 2. Hovmöller diagram of the spatio-temporal adjustments made to OH in the standard inversion set-up. The prior OH distribution, with respect to which changes are shown, is based on Spivakovsky et al. (2000), scaled down by a factor 0.92.

two, as it shares its emission distribution with the TM5OH inversion, and its OH distribution with the POP inversion. Contrastingly, the POP and TM5OH inversion share neither. This indicates convergence problems, rather than a significant influence from prior distributions. For reasons outlined in Section 3.5, we attribute differences in variations mostly to differences in the degree of convergence. Because the REF inversion resulted in the best match with observations (see Section 3.2), and because

185   the REF inversion is most consistent with a set of ten-year inversions (see Supplement S4), we consider it to be the solution that converged best.

As outlined in Section 2, we optimized OH in 45 latitude bands of 4° each. Figure 2 shows the adjustments in OH per latitude band through time, for the standard inversion. Clearly, adjustments to zonal mean OH can be much larger (up to 30%) than adjustments to annual global mean OH (up to 5%). Moreover, there is a strong systematic tendency to increase tropical

190   OH, and decrease extra-tropical OH, especially in the SH. This tendency was observed in each of the three inversion set-ups, i.e. also when a different OH field was used. We further investigate this tendency in Sections 3.2 and 3.4.
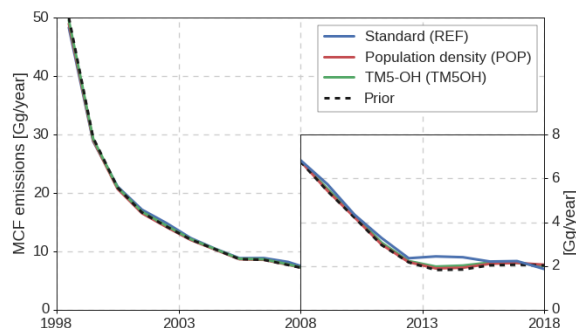
Figure 3. Timeseries of annual global total MCF emissions, derived in the three different inversion set-ups (solid lines) and the prior emissions (black dashed). To visualize variations in the low emissions in later years, we provide emissions in the second decade on a different y-scale (right axis).

The MCF emissions that result from the three inversions are shown in Figure 3. In general, emissions are increased relative to the prior, especially in later years. The REF inversion shows the largest adjustments and pronounced interannual variations, with even an increase in some years superimposed on the downward trend. Firstly, we note that the small emission totals in later years of around 2 Gg/yr, with interannual variations of 0.2 Gg/yr, would be hard to exclude from a bottom-up perspective. Secondly, the emission variations are uncorrelated with derived OH variations (r=0.13 in the REF inversion), which indicates that the MCF observations, to some degree, allow for independently derived OH and MCF emission variations. However, the contribution of the emission histories considered (Figure 3) to the MCF budget increases over the inversion period. Emissions are equivalent to 12% of the loss to OH from 2000 to 2006, but afterwards this ratio increases to up to 22% in 2017-18. Notably, we find that the emissions stabilize around 2 Gg/year in the final 5 years. Admittedly, this is partly driven by the assumed prior emissions (based on global mean MCF mole fractions), to which the inversion makes only small adjustments in later years. A growing relative contribution of emissions in the MCF budget would make derived OH variations more uncertain, especially if emission distributions had changed substantially over time. Therefore, even if high-quality measurements remain possible, residual MCF emissions could make it increasingly difficult to derive interannual changes in OH from MCF. Additionally, the uncertain decay rate of MCF emissions since 2001 (the last year with reported emissions) complicates the derivation of a trend of OH based on MCF observations.

3.2 Comparison to observations

3.2.1 NOAA surface network

Simulated global mean MCF mole fractions and the interhemispheric gradients in the posterior simulation match well with observed gradients (Figure 4). This illustrates the skill of the inverse framework to adjust emissions and OH such that large-scale gradients of MCF are very well ($< 1\%$) reproduced.
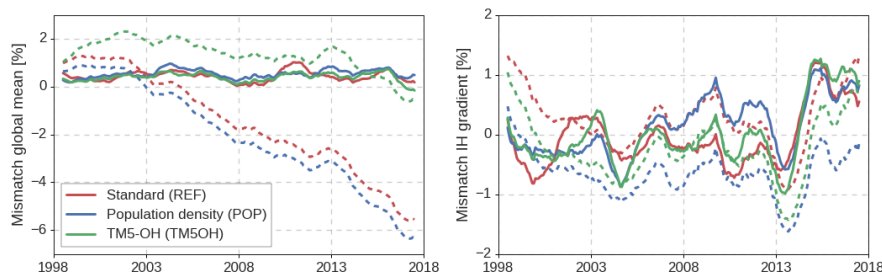
Figure 4. Fractional mismatch between simulated and observed MCF mole fractions in the global mean (left) and the interhemispheric gradient (right). Mismatches are given relative to global mean MCF and averaged using a twelve-month running mean. Dashed lines indicate prior mismatches, while solid lines show posterior mismatches. Global and hemispheric mean mole fractions were calculated from the NOAA surface network following the methods outlined in S1 of Naus et al. (2019).
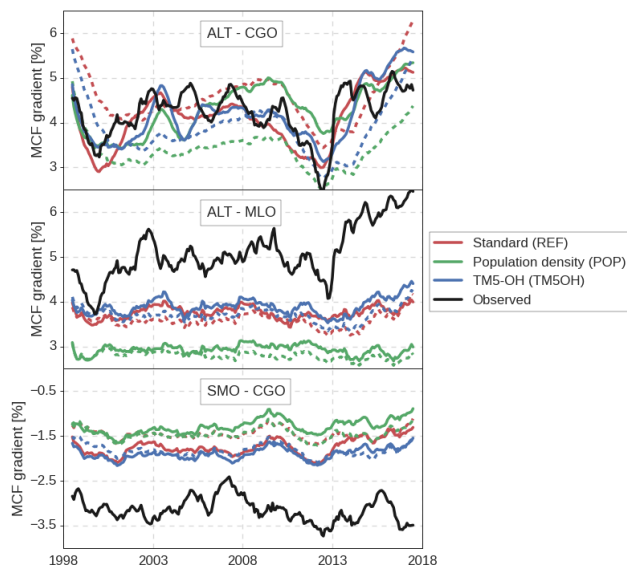
Figure 5. Timeseries of observed and modelled gradients between three sets of NOAA surface sites. Gradients are given relative to global mean MCF and averaged using a twelve-month running mean. Dashed lines indicate prior mismatches, while solid lines show posterior mismatches.

However, the inversion cannot reproduce some of the observed gradients between stations, especially gradients within hemispheres. In Figure 5, gradients between three pairs of NOAA surface sites are shown. Firstly, the interhemispheric gradient between ALT and CGO is captured well in all inversions. This interhemispheric gradient is strongly affected by emissions and therefore the inversion framework can adjust it with relative ease.
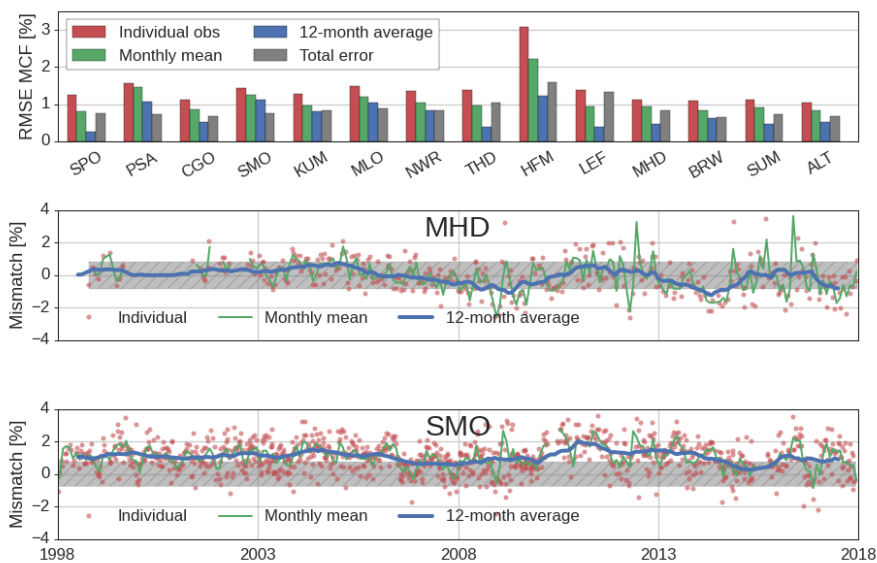
Figure 6. Top panel: Posterior root-mean-squared errors (RMSE) per surface site, for the REF inversion. RMSE are shown for individual observations, for monthly mean and for twelve-month running mean MCF mole fractions. Additionally, the site-dependent average total error that was used in the inversions, combined from a model and measurement error, is shown. RMSE are averages over the 1998-2018 inversion period and are given relative to the measured MCF mole fraction. Site abbreviations are explained in Table S1. Bottom two panels: Timeseries of the posterior measurement-model mismatch at MHD (top) and SMO (bottom) from individual observations, from monthly means and from twelve-month running averages, with the average total error shaded in gray.

In contrast, intrahemispheric gradients are less well captured. In Figure 5 it can be seen that both the gradient within the Northern Hemisphere, between ALT and MLO, and the gradient within the Southern Hemisphere, between SMO and CGO, are underestimated. More precisely, MCF mole fractions simulated at tropical sites are systematically too high (1-2 σ, with σ the total error), with a smaller, opposite bias at high-latitude sites (0.5-1 σ). The large latitudinal adjustments of OH (see Figure 2)

220 are an attempt by the inversion to reduce this bias, but the adjustments only reduce the bias partly (Figure 5). As an example, the SMO-CGO gradient is, in the REF inversion, increased from -1.5% to -2%, i.e. an increase of 30%, which corresponds well with a 30% latitudinal adjustment in OH. However, the observed gradient is larger still at -3%. We investigate this residual bias in more detail in Section 3.4.

We have quantified the skill of a simulation that uses optimized OH and MCF emission fields from the REF inversion to

225 reproduce observed MCF mole fraction in a root-mean-squared error (RMSE) per site, averaged over the 1998-2018 period (top panel in Figure 6). We distinguish between the RMSE of individual observations (as used in the optimization, in red), the RMSE of the monthly mean values (cyan), and the RMSE of twelve-month running averages (green). This helps to disentangle the contribution of short-term versus long-term variations to the model-measurement mismatch. Also shown is the pre-defined total observational error (gray), which we used in all inversions. The total error consists of a model error based on modelled
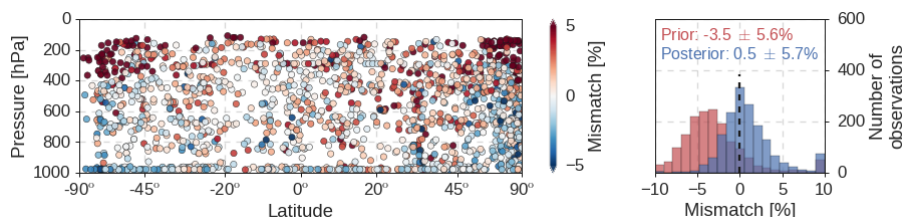
Figure 7. The mismatch of simulated minus observed MCF mole fractions from the HIPPO and ATom aircraft campaigns. Differences are shown relative to the observed mole fraction. We aggregated results from the HIPPO 1, 3- 5 and ATom 2 and 3 campaigns. Left: A plot of the model-measurement mismatches for each of the aircraft samples. Modelled mole fractions were sampled from the posterior REF simulation. Right: A probability-density distribution of the prior (red) and posterior (blue) mismatches in the REF inversion. Numbers denote the median mismatch and its standard deviation. Mismatches that fall outside the range on the x-axis were added to the outermost bars.

230 spatial gradients and a measurement error based on short-term measurement repeatability (see Section 2.2.1). Additionally, in the lower two panels, we visualize two examples of these mismatches for MHD, a somewhat polluted site with no residual bias, and for SMO, a relatively clean site with residual bias.

At all sites, the posterior RMSE of individual observations exceeds the total error. However, at most sites, the RMSE comes more in line with the total error for monthly means, and especially for twelve-month running averages. This implies that,

235 largely, the RMSE is related to short-term variations. Our inverse system, which employs relatively smooth and stiff OH and emission fields, has limited capability to fit short-term variations of MCF. Short-term variations in MCF are likely related to errors in the emission distribution and in small-scale transport, since OH has an integrated, slow effect on MCF mole fractions. Therefore, we do not expect these residuals to affect our OH estimate significantly. Importantly, we point out that our initial error estimate might have been overly conservative (mostly $< 1\%$, see Figure 6), which is supported by error estimates used

240 in previous MCF inversions (1-2% for individual observations (Bousquet et al., 2005); 5% for monthly, hemispheric averages (Turner et al., 2017; Rigby et al., 2017)). We conclude that, as long as we capture long-term variations of MCF at each site, the unresolved residuals on a sample-to-sample basis are unlikely to impact our conclusions. At some sites (notably SMO, MLO and PSA), we have identified systematic biases which are of more concern, and these result in relatively large RMSE even in twelve-month running averages. We further discuss systematic offsets in Section 3.4.

245 **3.2.2 HIPPO and ATom aircraft campaigns**

As the inversions were driven by observations from the NOAA surface network, we used the HIPPO and the ATom aircraft campaigns as independent data sources for validation. The main added value of the aircraft over surface observations is that the former provide snapshots of vertical gradients. When observed MCF mole fractions from all campaigns are compared to model-sampled mole fractions (Figure 7), a few features emerge.

250 Firstly, we find that the optimized REF simulation overestimates MCF mole fractions in the lower stratosphere at high latitudes ($> 50°$) in both hemispheres (left panel in Figure 7). This bias points to limited ability of TM5 to capture vertical

gradients in the downward branch of the Brewer-Dobson circulation. A similar bias was identified in TM5 simulations of CH_4, which has a stratospheric sink similar to MCF (Houweling et al., 2014).

In addition to the large overestimation at high altitudes, we also find a weak but significant positive correlation between altitude and model-measurement mismatch (R^2=0.12; p<0.001). Close to the surface, the average model-measurement mismatch is close to 0%, which increases to 1.5% at 10km. In other words, TM5 increasingly overestimates MCF mole fractions at higher altitudes, resulting in an underestimate of vertical gradients in TM5.

Positively, we find that the inversion improves the agreement between simulations and aircraft observations (right panel in Figure 7). While simulated mole fractions in the prior simulation are too low, in the posterior simulation MCF mole fractions compare well with observed mole fractions. The right panel in Figure 7 does show a distribution skewed towards model overestimation, which is linked to the overestimation in the lower stratosphere discussed above. While the average model-measurement difference decreases in the inversion, the standard deviation of the differences remains around 5%. This shows that vertically uniform adjustments in OH and in MCF emissions do not significantly modify simulated vertical gradients.

In conclusion, assimilation of surface observations improves agreement of our simulations with aircraft observations. However, modelled vertical gradients of MCF remain slightly smaller than those observed, although the maximum model bias is 1.5%, which is small compared to the 5% random error. Moreover, since these biases are consistent between the aircraft campaigns, we deem the impact of the biases on derived interannual and multi-annual variability of OH or MCF emissions small. Estimates of the total atmospheric oxidizing capacity are more likely to be affected by incorrect vertical transport. While TM5 typically compares well to other transport models in terms of large-scale transport features, for example in the Age of Air experiment (Krol et al., 2018), this comparison does highlight the crucial role of aircraft campaigns in helping to identify remaining transport model biases.

3.3 Physical drivers of OH variations

The El Niño Southern Oscillation (ENSO), a dominant mode of natural atmospheric variability, has previously been suggested to influence interannual variations in OH (Prinn et al., 2001; Turner et al., 2018). ENSO affects many processes that are linked to OH, such as temperature, atmospheric moisture, lightning, wildfires and atmospheric transport.

Figure 8 shows variations in ENSO, quantified in the Multivariate ENSO Index (MEI), together with the annual mean OH variations derived in the REF inversion. The correlation between the two is -0.30, or -0.57 if we let the MEI lead by one year. The correlation improves if we leave out 1998 as a spin-up year, since in 1998 we derive a positive OH anomaly coinciding with the an El Niño event, counter to the negative correlation we find over the rest of the timeseries. We note that the correlation is not driven by only a few outliers. Namely, if the outliers are removed (2010 and 2015), we still find correlations of -0.60, in that case even without a time lag. In general, we deem the negative correlation a robust property of the whole timeseries.

That variability in OH correlates with a dominant driver of atmospheric variability seems logical. However, attribution of the negative correlation to specific processes is difficult, given the large number of processes that are affected by ENSO and that in turn could affect OH. Nonetheless, we can hypothesize. For example, El Niño years (high MEI) are associated with more wildfires, resulting in higher CO emissions which could suppress OH concentrations (e.g., Nechita-Banda et al., 2018).
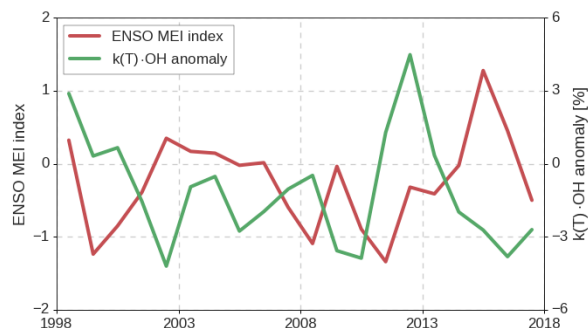
Figure 8. Variations in the annual mean ENSO MEI index (left axis) and variations in global, annual mean $k(T)\cdot$OH (right axis), as derived in the REF inversion.

La Niña years (low MEI) are associated with increased convection over the Pacific, increased lightning NO_x production and by extent increased OH recycling (Turner et al., 2018).

The correlation between MEI and the OH variations derived in a two-box model (Naus et al., 2019) is -0.01 if we do not tune the box model with a 3D transport model, and -0.34 if we do. This increase after accounting for some of the box model biases, and the even higher correlation if we move the inversion completely to a 3D transport model, shows that the correlation becomes apparent only when realistic transport of a 3D transport model is included. For example, transport variations related to ENSO have been shown to strongly affect interhemispheric differences of CO_2 (Francey and Frederiksen, 2016) and of CH_4 (Pandey et al., 2019), as well as mole fractions of MCF at SMO (Prinn et al., 1992).

3.4 Explaining the underestimated intrahemispheric gradients of MCF

The systematic underestimation of intrahemispheric gradients in both hemispheres deserves further elaboration, since the inversion framework has difficulties to adjust OH and emissions in such a way that intrahemispheric gradients are reproduced. MCF mole fractions are overestimated in the tropics and underestimated at high latitudes (Figure 5). To resolve these biases, the inversion introduces large adjustments in the latitudinal distribution of OH (up to 30%, see Figure 2). A set of inversions that only covered the 1998-2008 period were run to higher convergence (see Supplement S4). These inversions show that more extreme adjustments in the latitudinal OH distribution (up to 60%) better reproduce intrahemispheric gradients. However, intrahemispheric gradients were still not quite captured, and substantially higher MCF emissions were required to reproduce the gradients. The amplitude of these adjustments seem physically unlikely and in none of the inversions the biases were fully resolved. Therefore, we consider here alternative, or complimentary explanations for the biases, that were not explored in the inverse framework. We emphasize that the biases are quite constant over the twenty-year period, and while especially pronounced in the Southern Hemisphere, also present in the Northern Hemisphere. These aspects make anthropogenic emissions as a sole explanation unlikely.

One explanation for underestimated intrahemispheric gradients is that intrahemispheric mixing is too fast in TM5. Even after extensive participation of TM5 in intermodel comparisons (e.g., Krol et al., 2018), transport biases might persist. We have tested the effect of both horizontal (down to 1° x 1°) and vertical (up to 60 layers) model resolution on the simulated mole fractions (see Supplement S1). While we did find some sensitivity to resolution, the intrahemispheric biases persisted. Additionally, when we simulated SF_6, a chemically inert tracer commonly used for diagnosing large-scale transport (e.g., Patra et al., 1997; Denning et al., 1999), we did not find any comparable bias. Finally, we also simulated HFC-152a, a gas that is removed by OH against a shorter lifetime than MCF (~1.5 years (Ko et al., 2013)). For HFC-152a, we also found none of these biases. The results for SF_6 and HFC-152a are discussed more extensively in Supplement S2. We conclude that the biases seem particular to MCF and are therefore unlikely to be related to either transport or OH.

This leaves stratospheric photolysis, ocean-atmosphere exchange, another unknown MCF budget term, or a site-dependent measurement bias as potential explanations. Of these four, we consider the oceanic sink the likeliest. Wennberg et al. (2004) suggested that low MCF hydrolysis rates in cold, high-latitude oceans could result in a build-up of oceanic MCF. This reservoir would be released again when atmospheric mole fractions of MCF dropped, following production reductions demanded by the Montreal Protocol. They calculated and forecast the associated change in the ocean sink in five latitude bands for the period of 1961 to 2020 in a global ocean circulation model. We implemented their ocean flux in a forward simulation of MCF, and found that the adjusted ocean flux reduced the intrahemispheric bias by around 50% (see Supplement S3). This reduction is larger than the adjustments brought about by a 30% adjustment in tropical OH, and provides an arguably more likely scenario.

We also sampled aircraft observations in the simulation with an adjusted ocean flux. Release of MCF from high-latitude oceans would enhance vertical gradients, which combines well with the observation that TM5 underestimates aircraft-observed vertical gradients of MCF (see Section 3.2.2). However, we find that vertical gradients of MCF are only very slightly modified by the change in ocean flux, so that the signal of oceanic release of MCF in aircraft observations is too small to identify using the tools available to us.

Some new issues arise when we include the new ocean flux. Global mean MCF is overestimated, as the oceanic flux is much reduced, or even reversed. Additionally, the ALT to CGO gradient is captured less well. However, these are offsets that our inverse framework can resolve, as was found in Section 3.2.1. Therefore, we propose that variations in the oceanic flux of MCF very likely provide part of the solution to the residual intrahemispheric biases in our inversions. Further investigation of this issue, however, is beyond the scope of this study.

We note the dichotomy in the evidence for oceanic release of MCF. Positively, it emphasizes the resolving power of a sparse network of internally-consistent, low-frequency observations: we unexpectedly found a likely constraint on the oceanic uptake of MCF, in addition to the constraints on OH and emissions. Negatively, the existence of an ocean-atmosphere exchange of MCF, as opposed to a first-order sink, further increases uncertainty on any MCF-derived constraints on OH. Under the assumption that the exchange from Wennberg et al. (2004) is accurate, the impact of a different oceanic sink on derived interannual variations of OH has been shown to be small (Prinn et al., 2005). However, if the ocean-atmosphere exchange is assumed to be uncertain, then the similar spatial signature of the OH sink and ocean uptake (both high in the tropics) will make it difficult to resolve between the two using only the surface network. Still, given the continuous decline of MCF abundance

over our inversion period, no strong interannual variations in the ocean flux are expected. Therefore, variations in OH are still the most likely driver of interannual variations in MCF mole fractions, which we consider therefore a robust feature of our inversion. Contrastingly, uncertainty in the oceanic flux does complicate the derivation of a trend in OH from MCF observations, as well as spatial adjustments in the OH distribution. In other words, while we deem 30% adjustments in the OH distribution unlikely, we cannot exclude some underestimation of tropical OH as a partial explanation for the intrahemispheric biases.

3.5 The problem of convergence

Conventionally, the convergence criterion of a 4DVAR inversion is defined as a reduction in the cost function gradient. Ideally, the resulting converged state reproduces observations within the pre-defined total error. Due to pragmatic constraints, this procedure did not provide us with the desired result. Firstly, computational expense (∼3 iterations in two days) limited the number of iterations. Secondly, while further convergence was possible, the derived OH variations became less realistic physically. Two underlying problems have been pointed out: a difficulty in defining observational and model uncertainties and difficult-to-resolve intrahemispheric biases. However, while each of the three inversions faced these two problems, they did not reach the same level of convergence. For example, an emission distribution based on population density is more diffuse, and therefore contains more degrees of freedom than the TransCom emission distribution, but the TransCom distribution resulted in better convergence.

The importance of considering convergence when comparing the inverse results is illustrated by a set of inversions with the same set-up described in Section 2.1.2, but covering only 1998-2008. These ten-year inversions required less time per iteration and converged more consistently and in fewer iterations. The three ten-year inversions result in much more consistent interannual variations and spatial adjustments in OH, as described in more detail in Supplement S4. In turn, the interannual OH variations and the spatial OH adjustments derived in the ten-year inversions were most similar to those derived in the twenty-year REF inversion. This suggests that the converged solutions of the three inversions are likely to be similar, but that for unclear reasons the twenty-year REF inversion managed to converge furthest, while the other two either required more iterations, or reached a false minimum. In the ten-year inversions, tropical OH was increased by up to 60%, which helped to additionally reduce the intrahemispheric biases, although a residual bias remained. This all indicates that, while we managed to set-up and perform credible twenty-year global inversions in a 3D transport model, the inverse problem remains partly ill-posed.

4 Further discussion

An important question concerns the robustness of the derived OH variations. Our inversion procedure did not provide formal posterior uncertainties, but we did test the robustness of derived variations in sensitivity tests. Firstly, while we observed differences between the three inversion set-ups, we generally identified similar tendencies in each. Interannual variations in global oxidation and latitudinal adjustments in OH seem only marginally affected by the prior OH and emission distributions,

and most differences were driven by different degrees of convergence (see Section 3.5). Secondly, in a previous test inversion
375 where we only optimized one global monthly scaling factor for OH, interannual variations turned out similar. Thirdly, in a
forward simulation, we applied the interannual variations in oxidation to the prior OH distribution, i.e. without adjustments in
the spatial distribution. This resulted in a significantly improved match with observations compared to the interannual constant
prior, which means that the temporal variations in OH are important for reproducing the observations. These results indicate
substantial robustness of the derived OH variations.

380 Key to our inversions and the derived OH variations is the use of MCF observations from the NOAA-GML surface network.
MCF has additionally been monitored by the Advanced Global Atmospheric Gases Experiment (AGAGE) surface network
and its predecessors since 1978 (Prinn et al., 1983, 2018). Both networks maintain their own calibration scales for MCF, and
previous comparisons have revealed site-dependent scale drifts and a possible phase difference between the two networks
that exceed measurement repeatability (Holmes et al., 2013; Rigby et al., 2013). Due to these differences, and because of
385 different site locations and measurement approaches, an inversion incorporating AGAGE instead of NOAA observations will
result in different OH variations. It is difficult to assess the impact without performing additional inversions, but in a three-box
inverse system differences between interannual OH variations derived from each network were shown to be insignificant in the
presence of other uncertainties in the MCF budget (Rigby et al., 2017).

The only OH inversion studies that cover a similar period as this work were done in box models. As expected, the box model
390 inversion that gave interannual OH variations most similar to those presented here is from our previous work (Naus et al., 2019),
where we partly accounted for transport-related biases using TM5 ($R^2 = 0.49$; significant at p=0.01). This can be compared to
the two-box inversion where we did not account for these biases ($R^2 = 0.21$; not significant at p=0.01). We find similarly low
correlations with the OH variations derived in Turner et al. (2017) and in Rigby et al. (2017). In Section 3.3, we already noted
that the two-box inversion where we accounted for transport biases also correlated better with the ENSO cycle, while the OH
395 variations derived in this work correlate best with ENSO. This result, combined with the explicit simulation of transport and
the more extensive use of available data (e.g. site-to-site gradients) give us confidence that the OH variations derived in this
work are physically more realistic than those derived in two-box models. As such, we recommend the use of the OH variations
derived in our twenty-year REF inversion as an alternative to interannually repeating OH, or to OH derived in full-chemistry
simulations, in for example CH$_4$ inversions. We do note that the OH variations derived in this work are statistically consistent
400 with these previous studies, as uncertainties remain large relative to the amplitude of interannual variations in OH.

It remains difficult to derive a multi-annual trend in OH from an inversion of MCF. To facilitate convergence of our inversion,
we already pre-fitted MCF emissions to the global MCF trend. In principle spatially distinct patterns of emissions and OH still
allow for an OH trend in the posterior solution, but the signal of such an OH trend in MCF observations would be small.
Moreover, we have found evidence for a possible role of MCF release from oceans at high latitudes, as well as a growing
405 relative contribution of MCF emissions in the MCF budget. While we can leverage OH variations as the most likely source
of interannual variations in the MCF growth rate, variations in these other budget terms become more important on decadal
timescales. Therefore, on the basis of the inversions presented in this work, we conclude that a trend in OH cannot be excluded,
though we have found no evidence for such a trend in the MCF budget.

While MCF has been the most widely used tracer for observation-derived constraints on global mean OH over the past
decades, promising alternatives have been explored. ^{14}CO is produced from cosmic radiation in the stratosphere and subse-
quently transported to tropospheric surface sites (Quay et al., 2000). Observed variations of ^{14}CO could provide additional
constraints on OH, with a higher sensitivity to the tropics (Krol et al., 2008). Currently, long-term monitoring of ^{14}CO is lim-
ited to one site (Baring Head, New Zealand), but efforts are being made to expand the network (Petrenko et al., 2019). Recently,
it was proposed that high-resolution satellite data of CH_4 can be used to constrain both CH_4 sources and sinks, which would be
possible with a combination of satellite products with different vertical sensitivities (Maasakkers et al., 2019). Future research
will reveal how feasible this approach is, but it will not provide information retroactively, for past decades: here, surface data
still provides the strongest constraints. All potential tracers for OH are in principle complementary and the implementation of
multiple tracers in a comprehensive inversion framework could offer a more robust method for deriving OH variations (Liang
et al., 2017). Already, we have shown that tracers such as SF_6 and HFC-152a can help in understanding the role of OH in the
MCF budget. However, also in light of the results presented in this study, we deem it likely that each tracer will bring its own
complications, which should be considered with care. This makes a multi-tracer approach a promising, but complicated and
involving exercise.

Observational constraints have also been implemented in full-chemistry models. Assimilation of satellite data of those gases
that dominate the OH budget, such as CO and O_3, is likely to bring full-chemistry simulations closer to reality and makes them
less reliant on uncertain emission inventories (e.g., Miyazaki et al., 2012; Flemming et al., 2017). For example, assimilation
of CO satellite data in a full-chemistry simulation resulted in an enhanced positive trend in OH, compared to an unconstrained
simulation, which was driven predominantly by a decreasing atmospheric CO burden (Gaubert et al., 2017). An approach
complimentary to budget-based inverse modelling and full-chemistry simulations has been suggested in formaldehyde (HCHO)
(Wolfe et al., 2019). HCHO is well-monitored, both in-situ and by satellites, and the production of HCHO is tightly linked to
OH abundance, especially in the remote troposphere. This approach provides high-resolution information on the distribution
of OH. All these methods benefit from the availability of each of the other methods as independent validation. Therefore,
we consider that constraining the atmospheric oxidative capacity, a traditionally difficult problem at the heart of atmospheric
chemistry, potentially has a solution in the convergence of a growing number of independent lines of evidence that need
combined exploration.

5 Conclusions

In this study, we present a set of global 3D model inversions of MCF that cover the 1998-2018 period, performed within the
TM5-4DVAR inverse framework. In the inversions, MCF emissions and OH concentrations were optimized simultaneously,
with the objective to derive interannual variations in OH. The inverse system was typically able to reproduce observed MCF
mole fractions within 1%. The main conclusions of this work can be summarized as follows:

1. Small interannual variability (2-3%) of global mean OH without a significant trend allows for a relatively good match
   with MCF observations over the 1998−2018 period.

2. We have identified an underestimate of intrahemispheric gradients of MCF in the TM5 simulations that is not easily reduced using only adjustments in OH and anthropogenic MCF emissions. Instead, we propose that an explanation involving oceanic release of MCF at high latitudes can help to at least partly correct for these biases.

445

3. Most derived metrics, such as interannual OH variability and the absence of a trend in OH, are relatively robust with respect to the prior OH and emission distribution. However, we put the most confidence in interannual variations of OH, as trends and spatial adjustments of OH will be most strongly affected by remaining uncertainties in the system, such as the exact magnitudes of the oceanic flux and of anthropogenic emissions.

4. We find a significant and robust negative correlation between the derived variations in OH and the ENSO cycle. Such a

450

correlation was not found in box model studies that did not fully account for transport variations.

5. We suggest inclusion of our optimized global OH variations in global CH_4 inversions, since the timeseries of optimized OH better reproduces MCF observations than annually repeating OH. However, we emphasize that the solution remains very uncertain.

Data availability. Optimized OH and MCF emission fields derived in this study are available in the Supplemental Data. Additional results

455

are available on request. Flask observations of MCF, SF_6 and HFC-152a from the NOAA surface network, as well as flask observations from the HIPPO campaign that were used in this study, are available on ftp://ftp.cmdl.noaa.gov/hats/. Flask observations from the ATom campaign can be retrieved from https://daac.ornl.gov/.

Author contributions. MK, SN and SM designed the research. SN wrote the manuscript with major input from MK, and further contributions from all co-authors. SN performed the TM5 inversions and analysed the results. MK supervised the research. All authors discussed the results

460

and contributed to the final manuscript.

Competing interests. The authors declare that they have no conflict of interest.

Acknowledgements. This work was carried out on the Dutch National e-Infrastructure with the support of SURF Cooperative. This work was funded through the Netherlands Organisation for Scientific Research (NWO), project number 824.15.002. Maarten Krol received funding from the European Research Council (ERC) under the European Union's Horizon 2020 research and innovation programme under grant

465

agreement No 742798. Prabir K. Patra is partly supported by Environment Research and Technology Development Fund (#2-1802) of the Ministry of the Environment, Japan. We thank the NOAA and cooperative station personnel for diligence and care in the collection of flasks. We thank C. Siso and B. Miller for assistance with analysis of ground-station flasks and flasks collected during aircraft campaigns, F. Moore

and E. Atlas for assistance with flask sampling during HIPPO and ATom, and the broader NSF and NOAA teams for enabling and facilitating those projects.

470 **References**

Bergamaschi, P., Frankenberg, C., Meirink, J. F., Krol, M., Villani, M. G., Houweling, S., Dentener, F., Dlugokencky, E. J., Miller, J. B., Gatti, L. V., Engel, A., and Levin, I.: Inverse modeling of global and regional CH_4 emissions using SCIAMACHY satellite retrievals, Journal of Geophysical Research: Atmospheres, 114, 2009.

Bousquet, P., Hauglustaine, D. A., Peylin, P., Carouge, C., and Ciais, P.: Two decades of OH variability as inferred by an inversion of
475   atmospheric transport and chemistry of methyl chloroform, Atmospheric Chemistry and Physics, 5, 2635–2656, 2005.

Brühl, C. and Crutzen, P. J.: MPIC two-dimensional model, NASA Ref. Publ, 1292, 103–104, 1993.

Burkholder, J. B., Sander, S. P., Abbatt, J. P. D., Barker, J. R., Huie, R. E., Kolb, C. E., Kurylo, M. J., Orkin, V. L., Wilmouth, D. M., and Wine, P. H.: Chemical kinetics and photochemical data for use in atmospheric studies: evaluation number 18, Tech. rep., Pasadena, CA: Jet Propulsion Laboratory, National Aeronautics and Space . . . , 2015.

480 Chipperfield, M. P. and Liang, Q. e. a.: Model estimates of lifetimes, in: SPARC, 2013: SPARC Report on the Lifetimes of Stratospheric Ozone-Deleting Substances, Their Replacements, and Related Species, edited by Reimann, S., Ko, M. K. W., Newman, P. A., and Strahan, S. E., chap. 5, WCRP-15/2013, 2013.

CIESIN, Columbia University: Gridded Population of the World, Version 4 (GPWv4): Population Density, Revision 11., https://doi.org/https://doi.org/10.7927/H49C6VHW, 2018.

485 Dee, D. P., Uppala, S. M., Simmons, A. J., Berrisford, P., Poli, P., Kobayashi, S., Andrae, U., Balmaseda, M. A., Balsamo, G., Bauer, P., et al.: The ERA-Interim reanalysis: Configuration and performance of the data assimilation system, Quarterly Journal of the royal meteorological society, 137, 553–597, 2011.

Denning, A. S., Holzer, M., Gurney, K. R., Heimann, M., Law, R. M., Rayner, P. J., Fung, I. Y., Fan, S.-M., Taguchi, S., Friedlingstein, P., et al.: Three-dimensional transport and concentration of SF_6: A model intercomparison study (TransCom 2), Tellus B: Chemical and
490   Physical Meteorology, 51, 266–297, 1999.

Flemming, J., Benedetti, A., Inness, A., Engelen, R. J., Jones, L., Huijnen, V., Remy, S., Parrington, M., Suttie, M., Bozzo, A., Peuch, V.-H., Akritidis, D., and Katragkou, E.: The CAMS interim Reanalysis of Carbon Monoxide, Ozone and Aerosol for 2003–2015, Atmospheric Chemistry and Physics, 17, 1945–1983, https://doi.org/10.5194/acp-17-1945-2017, https://www.atmos-chem-phys.net/17/1945/2017/, 2017.

495 Francey, R. J. and Frederiksen, J. S.: The 2009-2010 step in atmospheric CO_2 interhemispheric difference, Biogeosciences, 13, 873, 2016.

Gaubert, B., Worden, H. M., Arellano, A. F. J., Emmons, L. K., Tilmes, S., Barré, J., Martinez Alonso, S., Vitt, F., Anderson, J. L., Alkemade, F., Houweling, S., and Edwards, D. P.: Chemical feedback from decreasing carbon monoxide emissions, Geophysical Research Letters, 44, 9985–9995, 2017.

Gilbert, J. C. and Lemaréchal, C.: Some numerical experiments with variable-storage quasi-Newton algorithms, Mathematical programming,
500   45, 407–435, 1989.

Holmes, C. D., Prather, M. J., Søvde, O. A., and Myhre, G.: Future methane, hydroxyl, and their uncertainties: key climate and emission parameters for future predictions, Atmospheric Chemistry and Physics, 13, 285–302, 2013.

Houweling, S., Krol, M., Bergamaschi, P., Frankenberg, C., Dlugokencky, E. J., Morino, I., Notholt, J., Sherlock, V., Wunch, D., Beck, V., Gerbig, C., Chen, H., Kort, E. A., Röckmann, T., and Aben, I.: A multi-year methane inversion using SCIAMACHY, accounting
505   for systematic errors using TCCON measurements, Atmospheric Chemistry and Physics, 14, 3991–4012, https://doi.org/10.5194/acp-14-3991-2014, https://www.atmos-chem-phys.net/14/3991/2014/, 2014.

Huijnen, V., Williams, J., Weele, M. v., Noije, T. v., Krol, M. C., Dentener, F., Segers, A., Houweling, S., Peters, W., Laat, J. d., et al.: The global chemistry transport model TM5: description and evaluation of the tropospheric chemistry version 3.0, Geoscientific Model Development, 3, 445–473, 2010.

510   Ko, M. K. W., Newman, P. A., Reimann, S., and Strahan, S. E.: SPARC report on the lifetimes of stratospheric ozone-depleting substances, their replacements, and related species, SPARC Report No. 6, 2013.

Krol, M., Houweling, S., Bregman, B., Broek, M., Segers, A., Velthoven, P. v., Peters, W., Dentener, F., and Bergamaschi, P.: The two-way nested global chemistry-transport zoom model TM5: algorithm and applications, Atmospheric Chemistry and Physics, 5, 417–432, 2005.

Krol, M., de Bruine, M., Killaars, L., Ouwersloot, H., Pozzer, A., Yin, Y., Chevallier, F., Bousquet, P., Patra, P., Belikov, D., Maksyutov, S.,

515   Dhomse, S., Feng, W., and Chipperfield, M. P.: Age of air as a diagnostic for transport timescales in global models, Geoscientific Model Development, 11, 3109–3130, https://doi.org/10.5194/gmd-11-3109-2018, https://www.geosci-model-dev.net/11/3109/2018/, 2018.

Krol, M. C., Meirink, J. F., Bergamaschi, P., Mak, J. E., Lowe, D., Jöckel, P., Houweling, S., and Röckmann, T.: What can [14]CO measurements tell us about OH?, Atmospheric chemistry and physics, 8, 5033–5044, 2008.

Lawrence, M. G., Jöckel, P., and Kuhlmann, R. v.: What does the global mean OH concentration tell us?, Atmospheric Chemistry and

520   Physics, 1, 37–49, 2001.

Liang, Q., Chipperfield, M. P., Fleming, E. L., Abraham, N. L., Braesicke, P., Burkholder, J. B., Daniel, J. S., Dhomse, S., Fraser, P. J., Hardiman, S. C., et al.: Deriving Global OH Abundance and Atmospheric Lifetimes for Long-Lived Gases: A Search for CH_3CCl_3 Alternatives, Journal of Geophysical Research: Atmospheres, 2017.

Lovelock, J. E.: Methyl chloroform in the troposphere as an indicator of OH radical abundance, Nature, 267, 32–32, 1977.

525   Maasakkers, J. D., Jacob, D. J., Sulprizio, M. P., Scarpelli, T. R., Nesser, H., Sheng, J.-X., Zhang, Y., Hersher, M., Bloom, A. A., Bowman, K. W., Worden, J. R., Janssens-Maenhout, G., and Parker, R. J.: Global distribution of methane emissions, emission trends, and OH concentrations and trends inferred from an inversion of GOSAT satellite data for 2010–2015, Atmospheric Chemistry and Physics, 19, 7859–7881, https://doi.org/10.5194/acp-19-7859-2019, https://www.atmos-chem-phys.net/19/7859/2019/, 2019.

Meirink, J. F., Bergamaschi, P., and Krol, M. C.: Four-dimensional variational data assimilation for inverse modelling of atmospheric methane

530   emissions: method and comparison with synthesis inversion, Atmospheric chemistry and physics, 8, 6341–6353, 2008.

Miyazaki, K., Eskes, H. J., Sudo, K., Takigawa, M., van Weele, M., and Boersma, K. F.: Simultaneous assimilation of satellite NO_2, O_3, CO, and HNO_3 data for the analysis of tropospheric chemical composition and emissions, Atmospheric Chemistry and Physics, 12, 9545–9579, https://doi.org/10.5194/acp-12-9545-2012, https://www.atmos-chem-phys.net/12/9545/2012/, 2012.

Montzka, S. A., Spivakovsky, C. M., Butler, J. H., Elkins, J. W., Lock, L. T., and Mondeel, D. J.: New observational constraints for atmo-

535   spheric hydroxyl on global and hemispheric scales, Science, 288, 500–503, 2000.

Montzka, S. A., Krol, M., Dlugokencky, E. J., Hall, B., Jöckel, P., and Lelieveld, J.: Small interannual variability of global atmospheric hydroxyl, Science, 331, 67–69, 2011.

Naus, S., Montzka, S. A., Pandey, S., Basu, S., Dlugokencky, E. J., and Krol, M.: Constraints and biases in a tropospheric two-box model of OH, Atmospheric Chemistry and Physics, 19, 407–424, 2019.

540   Nechita-Banda, N., Krol, M., Van Der Werf, G. R., Kaiser, J. W., Pandey, S., Huijnen, V., Clerbaux, C., Coheur, P., Deeter, M. N., and Röckmann, T.: Monitoring emissions from the 2015 Indonesian fires using CO satellite data, Philosophical Transactions of the Royal Society B: Biological Sciences, 373, 20170 307, 2018.

Pandey, S., Houweling, S., Krol, M., Aben, I., Nechita-Banda, N., Thoning, K., Röckmann, T., Yin, Y., Segers, A., and Dlugokencky, E. J.:
Influence of atmospheric transport on estimates of variability in the global methane burden, Geophysical Research Letters, 46, 2302–2311,
2019.

Patra, P. K., Lal, S., Subbaraya, B. H., Jackman, C. H., and Rajaratnam, P.: Observed vertical profile of sulphur hexafluoride (SF_6) and its
atmospheric applications, Journal of Geophysical Research: Atmospheres, 102, 8855–8859, 1997.

Patra, P. K., Takigawa, M., Ishijima, K., Choi, B.-C., Cunnold, D., Dlugokencky, E. J., Fraser, P., Gomez-Pelaez, A. J., Goo, T.-Y., Kim, J.-S.,
et al.: Growth rate, seasonal, synoptic, diurnal variations and budget of methane in the lower atmosphere, Journal of the Meteorological
Society of Japan. Ser. II, 87, 635–663, 2009.

Patra, P. K., Houweling, S., Krol, M. C., Bousquet, P., Belikov, D., Bergmann, D., Bian, H., Cameron-Smith, P., Chipperfield, M. P., Corbin,
K., et al.: TransCom model simulations of CH_4 and related species: linking transport, surface flux and chemical loss with CH_4 variability
in the troposphere and lower stratosphere, Atmospheric Chemistry and Physics, 11, 12813–12837, 2011.

Patra, P. K., Krol, M. C., Montzka, S. A., Arnold, T., Atlas, E. L., Lintner, B. R., Stephens, B. B., Xiang, B., Elkins, J. W., Fraser, P. J., et al.:
Observational evidence for interhemispheric hydroxyl-radical parity, Nature, 513, 219–223, 2014.

Petrenko, V., Murray, L., Smith, A., Crosier, E., Colton, A., Hua, Q., Yang, B., Kazemi, R., Neff, P., Etheridge, D., Usoskin, I., and Poluianov,
S.: Using atmospheric ^{14}CO to provide additional constraints for global OH: results from a new approach and potential for future mea-
surements., in: Geophysical Research Abstracts, vol. 21, 2019.

Prinn, R., Cunnold, D., Rasmussen, R., Simmonds, P., Alyea, F., Crawford, A., Fraser, P., and Rosen, R.: Atmospheric trends in methylchlo-
roform and the global average for the hydroxyl radical, Science, 238, 945–950, 1987.

Prinn, R., Cunnold, D., Simmonds, P., Alyea, F., Boldi, R., Crawford, A., Fraser, P., Gutzler, D., Hartley, D., Rosen, R., et al.: Global average
concentration and trend for hydroxyl radicals deduced from ALE/GAGE trichloroethane (methyl chloroform) data for 1978–1990, Journal
of Geophysical Research: Atmospheres, 97, 2445–2461, 1992.

Prinn, R. G., Simmonds, P. G., Rasmussen, R. A., Rosen, R. D., Alyea, F. N., Cardelino, C. A., Crawford, A. J., Cunnold, D. M., Fraser,
P. J., and Lovelock, J. E.: The atmospheric lifetime experiment: 1. Introduction, instrumentation, and overview, Journal of Geophysical
Research: Oceans, 88, 8353–8367, 1983.

Prinn, R. G., Huang, J., Weiss, R. F., Cunnold, D. M., Fraser, P. J., Simmonds, P. G., McCulloch, A., Harth, C., Salameh, P., O'Doherty,
S., Wang, R. H. J., Porter, L., and Miller, B. R.: Evidence for Substantial Variations of Atmospheric Hydroxyl Radicals in the Past Two
Decades, Science, 292, 1882–1888, https://doi.org/10.1126/science.1058673, 2001.

Prinn, R. G., Huang, J., Weiss, R. F., Cunnold, D. M., Fraser, P. J., Simmonds, P. G., McCulloch, A., Harth, C., Reimann, S., Salameh, P.,
et al.: Evidence for variability of atmospheric hydroxyl radicals over the past quarter century, Geophysical Research Letters, 32, 2005.

Prinn, R. G., Weiss, R. F., Arduini, J., Arnold, T., DeWitt, H. L., Fraser, P. J., Ganesan, A. L., Gasore, J., Harth, C. M., Hermansen, O., et al.:
History of chemically and radiatively important atmospheric gases from the Advanced Global Atmospheric Gases Experiment (AGAGE),
Earth System Science Data, 10, 985–1018, 2018.

Quay, P., King, S., White, D., Brockington, M., Plotkin, B., Gammon, R., Gerst, S., and Stutsman, J.: Atmospheric ^{14}CO: A tracer of OH
concentration and mixing rates, Journal of Geophysical Research: Atmospheres, 105, 15147–15166, 2000.

Rigby, M., Prinn, R. G., O'Doherty, S., Montzka, S. A., McCulloch, A., Harth, C. M., Mühle, J., Salameh, P. K., Weiss, R. F., Young, D.,
et al.: Re-evaluation of the lifetimes of the major CFCs and CH_3CCl_3 using atmospheric trends, Atmospheric Chemistry and Physics, 13,
2691–2702, 2013.

580   Rigby, M., Montzka, S. A., Prinn, R. G., White, J. W. C., Young, D., O'Doherty, S., Lunt, M. F., Ganesan, A. L., Manning, A. J., Simmonds, P. G., et al.: Role of atmospheric oxidation in recent methane growth, Proceedings of the National Academy of Sciences, 114, 5373–5377, 2017.

Spivakovsky, C. M., Logan, J. A., Montzka, S. A., Balkanski, Y. J., Foreman-Fowler, M., Jones, D. B. A., Horowitz, L. W., Fusco, A. C., Brenninkmeijer, C. A. M., Prather, M. J., et al.: Three-dimensional climatological distribution of tropospheric OH: Update and evaluation,

585   Journal of Geophysical Research: Atmospheres, 105, 8931–8980, 2000.

Turner, A. J., Frankenberg, C., Wennberg, P. O., and Jacob, D. J.: Ambiguity in the causes for decadal trends in atmospheric methane and hydroxyl, Proceedings of the National Academy of Sciences, p. 201616020, 2017.

Turner, A. J., Fung, I., Naik, V., Horowitz, L. W., and Cohen, R. C.: Modulation of hydroxyl variability by ENSO in the absence of external forcing, Proceedings of the National Academy of Sciences, 115, 8931–8936, 2018.

590   Wennberg, P. O., Peacock, S., Randerson, J. T., and Bleck, R.: Recent changes in the air-sea gas exchange of methyl chloroform, Geophysical research letters, 31, 2004.

Wofsy, S., Afshar, S., Allen, H., APEL, E., Asher, E., Barletta, B., Bent, J., Bian, H., Biggs, B., Blake, D., et al.: ATom: Merged atmospheric chemistry, trace gases, and aerosols, ORNL DAAC, 2018.

Wofsy, S. C., the HIPPO science team, cooperating modellers, and satellite teams: HIAPER Pole-to-Pole Observations (HIPPO): fine-grained,

595   global-scale measurements of climatically important atmospheric gases and aerosols, Philosophical Transactions of the Royal Society of London A: Mathematical, Physical and Engineering Sciences, 369, 2073–2086, 2011.

Wolfe, G. M., Nicely, J. M., Clair, J. M., Hanisco, T. F., Liao, J., Oman, L. D., Brune, W. B., Miller, D., Thames, A., Abad, G. G., Ryersong, T. B., Thompsong, C. R., Peischlg, J., McKainh, K., Sweeney, C., Wennberg, P. O., Kim, M., Crounse, J. D., Hall, S. R., Ullman, K., Diskin, G., Buin, P., Chang, C., and J., D.-D.: Mapping hydroxyl variability throughout the global remote troposphere via synthesis of

600   airborne and satellite formaldehyde observations, Proceedings of the National Academy of Sciences, 116, 11 171–11 180, 2019.